

# Intra-subject Elastic Registration of 3D Ultrasound Images

Pezhman Foroughi<sup>a</sup>, Purang Abolmaesumi<sup>a,b,\*</sup>  
and Keyvan Hashtrudi-Zaad<sup>a</sup>

<sup>a</sup>*Department of Electrical and Computer Engineering, Queen's University,  
Canada,*

<sup>b</sup>*School of Computing, Queen's University, Canada.*

---

## Abstract

3D registration of ultrasound images is an important and fast-growing research area with various medical applications, such as image-guided radiotherapy and surgery. However, this registration process remains extremely challenging due to the deformation of soft tissue and the existence of speckles in these images. This paper presents a technique for intra-subject, intra-modality elastic registration of 3D ultrasound images. Using the general concept of attribute vectors, we define the corresponding voxels in the fixed and moving images. Our method does not require presegmentation and does not employ any numerical optimization procedure. As the computational requirements are minimal, the method has potential use in real-time applications. The technique is implemented and tested on 3D ultrasound images of human liver, captured by a 3D ultrasound transducer. The results show that the method is sufficiently accurate and robust even in cases where artifacts such as shadows exist in the ultrasound data.

*Key words:*

Image registration, 3D ultrasound, elastic registration, soft-tissue deformation, attribute vector.

---

## 1 Introduction

Ultrasound is an easy-to-use, inexpensive and real-time imaging tool, with no ionizing radiation, which is widely utilized in diagnosis applications. It is often employed to scan soft tissues such as the liver, kidneys and pancreas.

---

\* Corresponding author: purang@cs.queensu.ca

The soft tissues are easily deformed during scanning, mainly because of transducer pressure, respiration, and heartbeat. Determination of this nonrigid deformation is crucial for real-time applications such as image-guided surgery, radiotherapy, and robot-assisted biopsy. Intra-operative registration may be employed to compensate for patient's breathing, or to track a tumor. Furthermore, ultrasound registration could be used to measure tissue mechanic properties. However, due to speckles, shadowing effects and the poor quality of the images, the registration of this imaging modality is a challenging process especially for large nonrigid deformations. Consequently, the research on intra-modality registration of ultrasound images is very limited in the literature, but there appears to be an accrued interest in work related to the application of ultrasound images (Pluim and Fitzpatrick (2003)). Previous attempts include the development of techniques for the registration of ultrasound to other image modalities such as CT and MRI (Blackall et al. (2005); Letteboer et al. (2005); Aylward et al. (2002); King et al. (2001); Arbel et al. (2001); King et al. (2000); Pagoulatos et al. (1999); Maintz and Viergever (1998)), as well as intra-modality registration of ultrasound images discussed in the following. General information on registration of other modalities can be found in Hill et al. (2001); Hajnal et al. (2001); Maintz and Viergever (1998).

As the deformation of soft tissue is not guaranteed to occur in the plane scanned by the ultrasound beam, 2D registration of ultrasound images is not sufficiently robust for most clinical applications. The anatomical features might appear or disappear in the 2D images as a result of out-of-plane movement. Thanks to techniques such as free-hand 3D ultrasound reconstruction and newly developed 3D ultrasound transducers, there has been growing interest in the registration of 3D ultrasound images. The following introduces some of the prior art on intra-modality registration of ultrasound images especially the 3D nonrigid techniques. The type of registration (Rigid, Affine, Elastic, etc.), the targeted application, the validation experiments and the results of each method are briefly discussed.

Rohling et al. (1998) rigidly registered the reconstructed 3D ultrasound images of human gall bladder to exploit spatial compounding in order to improve the quality of 3D ultrasound data. The correlation of the gradient magnitude data of the two volumes is maximized to find the registration parameters. It is shown that spatially compounded datasets yield better segmentation results. The algorithm was limited only to applications where rigid-body registration would provide acceptable accuracy and where computational time in the order of hours was reported.

Shekhar and Zagrodsky (2002) investigated the registration of ultrasound volumes, based on the mutual information measure. Median filter was found to be the proper smoothing filter for this method. Intensity quantization was shown to increase the signal-to-noise ratio, and robust optimization behavior was

achieved using trilinear partial volume distribution interpolation. The method was applied to rigid-body transformation with both uniform and nonuniform scaling as well as to affine transformation. To evaluate the method, the deformations were applied to five volume pairs of cardiac ultrasound data. The results, only reported for simulated deformations applied to the ultrasound data, demonstrate a large capture range, high accuracy, and execution times in the order of 16-24 min for rigid body registration on volumes with the size of  $128 \times 128 \times 512$  voxels and in the order of minutes for volumes with the size of  $64 \times 64 \times 256$  voxels (*note*: to fairly compare computation time mentioned in each referenced article, one has to consider the platform algorithm has been implemented on).

In another study, Krucker et al. (2002) developed a subvolume-based algorithm for elastic ultrasound registration. The image was divided into subvolumes interactively, and local rigid registrations were computed. Connectivity of the entire volume was ensured by global interpolation using thin-plate splines after each iteration. At the first stage, a global affine registration was optionally determined using MIAMI Fuse<sup>©</sup> software (Meyer et al. (1997)). The performance was tested on synthetic deformations of 1.5-2.5 mm and two phantom scans, simulating the deformations in breast images. In this approach, the average deformation of 1.01 mm between the two volumes was reduced to 0.30 mm. The algorithm computation time was reported to be below 5 min for ultrasound volumes as large as 13 MB. No result was reported for larger initial average displacements. The subvolume-based approach was also employed for spatial compounding and extended field-of-view (Poon and Rohling (2006); Groves and Rohling (2004)).

Investigating a correlation-based approach, Xiao et al. (2002) registered 3D free-hand ultrasound images of breast using a block-matching scheme. The reference image was sampled at a set of grid points. Each sample comprised a block of voxels centered on a grid point. The best match for the block was subsequently located within a 3D search window. The compounding results of two sweeps before and after registration were reported. The algorithm was tested on real breast cyst images, with initial deformations of only a few millimeters, and computational time in the order of minutes was reported.

Deformable registration of cardiac images has been investigated more specifically in Ledesma-Carbayo et al. (2001); Shekhar et al. (2004); Makela et al. (2002). Considering elastic registration as an optimization problem, Ledesma-Carbayo et al. (2001) elastically registered the 2D sequences of cardiac images by optimizing a sum of squared differences with respect to the coefficients of splines. Shekhar et al. (2004) is a continuation of work reported in Shekhar and Zagrodsky (2002), however no specific information was provided on the computational complexity of the algorithm. 3D-ultrasound registration has also been targeted for brain shift correction. In Pratikakis et al. (2001), reg-

istration was defined as a motion estimation problem. A cost function was minimized in a multi-scale framework. A coarse-to-fine registration approach was proposed and tested on only one 3D ultrasound volume of an 8-month old baby. No detailed analysis was forthcoming as to the execution time of the technique.

In this paper, we present a new intra-subject, intra-modality elastic registration technique of 3D ultrasound images. The algorithm is designed to be automatic, fast and computationally efficient, therefore potentially applicable for real-time image-guided surgery and radiotherapy. The current paper builds upon our earlier report (Foroughi and Abolmaesumi (2005)) and provides a rigorous examination and analysis of the accuracy and performance of the algorithm implemented on real 3D ultrasound datasets. Under our approach, the concept of attribute vectors is employed to find corresponding voxels in the two ultrasound volumes being registered. Using the attribute vectors, a set of leading points is automatically selected in the deformed image (referred to as moving image), and the corresponding points are found in the reference or base image (referred to as fixed image). Finally, the moving image is warped into the fixed image. The registration results on human liver images show that the algorithm is accurate for initial deformations in the order of one centimeter with computational time of 3 minutes or less on a conventional PC.

Our approach although similar to that of HAMMER (Shen and Davatzikos (2002); Shen (2004)), which was originally proposed for the registration of MRI images of human brain, specifically differs in the following: 1) The computational time of the HAMMER technique has been reported to be in the order of hours, which is not acceptable for real-time clinical applications. The high computational cost is attributable to the calculation of Geometric Moment Invariant (GMI) attribute vector elements and to the employment of an iterative optimization in the registration process. To reduce the computation time, we propose a new set of elements for the attribute vector and eliminate the numerical optimization phase in our implementation. We demonstrate that our new attribute vector produces superior registration results in the case of ultrasound images, compared to the results achieved by using GMIs. Furthermore, the registration accuracy is sufficient for the majority of clinical applications, without the employment of the iterative phase; 2) Our energy function is simpler than the one used in HAMMER, and this also reduces our computational complexity; and 3) A different warping method is employed to consider a more nonuniform distribution of leading points in the ultrasound images of human liver in comparison to the MRI images of brain.

This paper is organized as follows. Section 2 outlines the methodology and details of the implementation. Experimental results on 3D liver images are presented in Section 3. Section 4 discusses the sensitivity of the algorithm performance to the effect of parameters, and provides a comparison with the

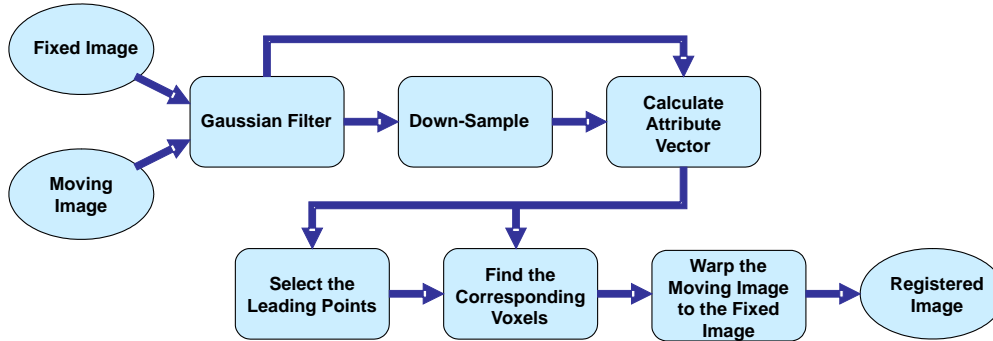


Fig. 1. The registration process

GMI-based feature vectors. Section 5 concludes the paper and presents the future work.

## 2 Methodology

The proposed algorithm is demonstrated in Figure 1. Initially, both fixed and moving images are passed through a Gaussian filter with the size of  $7 \times 7 \times 7$  voxels. This filter is an anti-aliasing filter for down-sampled images which reduces the effect of speckles. In the next step, the elements of attribute vectors are calculated in two different scales for each voxel in both fixed and moving images. Then, the leading points with the highest magnitude attribute vectors are selected and registered, and finally the moving image is warped to the fixed image. The following paragraphs explain these steps in detail.

### 2.1 Attribute Vectors

We used the concept of attribute vectors introduced in Shen (2004), to extract corresponding feature points from the two ultrasound images being registered. In Shen (2004), geometric moment invariants (GMIs), calculated from local spatial intensity histograms, form the attribute vector which is assigned to each voxel in the image. Each attribute vector reflects the underlying anatomy and distinguishes different features in an image.

Due to the presence of speckles in ultrasound images, our experiments show that GMIs do not generate robust attribute vectors, as they mainly characterize the speckle pattern (see Section 4.4). Depending on the properties of the imaging modality, other elements could be selected for the attribute vector. Our proposed method replaces GMIs with a set of new elements that we found to work better for ultrasound images.

The new elements of our attribute vector are the intensity of the voxel, the magnitude of the gradient, and the Laplacian of the Gaussian (LoG). Each element of the suggested attribute vector emphasizes the properties of the underlying anatomy. The intensity guarantees that the bright voxels will not be registered to the dark ones and vice versa. The magnitude of gradient and LoG emphasize the edges and ridges inside the images, and reveal the boundary information of features in the images. The gradient is previously used for registration of ultrasound images, and is shown to be a suitable choice (Rohling et al. (1998)). The images, however, should be filtered before computing their derivatives. The LoG values are employed to locate features that surround smooth or faded soft transitions in ultrasound images.

In our implementation, the gradient and LoG values were calculated in the spatial domain with masks of the size of  $3 \times 3 \times 3$  voxels. All elements are calculated using two scales, resulting in an attribute vector with six elements. The elements from the down-sampled image capture general specifications of the anatomy, whereas the ones computed from the full-size image depict more detailed features. The LoG values are normalized between -0.5 and 0.5, and all other elements are normalized between zero and one in order to fit the similarity function, described in Section 2.3. The normalization is linear and global for each image. The variance of each element could also be used in the normalization process, however it is not considered in the current implementation.

Since the values of the gradient and LoG are calculated in two different scales, we have separated the Gaussian pre-filtering stage from the calculation of these values because of computation speed concerns. Obviously, one could condense these two stages into one step, and eliminate the pre-filtering stage. However, the size of the filters for calculation of each element of the attribute vector would increase to  $7 \times 7 \times 7$ , making the overall process less efficient.

## *2.2 Leading Point Selection*

One of the major advantages of our proposed technique is its fast computational speed. To this end, instead of searching for corresponding voxel points for all the voxels within the moving and fixed image data sets, the algorithm automatically selects distinct major features of the moving image and registers them to the fixed image. The displacement of the rest of the voxel points is simply calculated based on the displacement of major feature points. As mentioned above, our attribute vectors consider the intensity, as well as the first and the second order derivatives of the image, since we expect the edges and ridges to be reliably identified in the fixed and moving data sets. Therefore, our leading point selection process is based on identifying feature points

in the ultrasound data that are mostly distributed around these strong visual features. This selection process includes the calculation of an *importance function* for each voxel. The importance of voxel  $v$  is simply defined as

$$im(v) = \sum_{i=1}^n (w_i \times \|e_i(v)\|), \quad (1)$$

where  $e_i(v)$  is the  $i$ 'th element of attribute vector at point  $v$ ,  $n$  is the number of elements of attribute vector, and  $w_i$  is the weight designated for the  $i$ 'th element.  $w_i$ 's are selected such that more emphasis is given to the feature points that reside on edges in ultrasound images, as, visually, these points can be more reliably identified in the moving and fixed data sets in the set of images we used for our experiments. Therefore,  $w_i$  values for the intensity and LoG are chosen to be one, whereas  $w_i$  for the gradient element is selected to be two in the current implementation. As described in Equation (1), the weighted absolute values of the elements of the attribute vector are summed up for each voxel. Those points with an importance function greater than a threshold are selected as leading points. An analysis of the sensitivity of the algorithm to the threshold values is provided in Section 4.1.

In our approach, the selected leading points are processed in descending order based on the values assigned from Equation (1) to each of them. Once a leading point is selected, no more points within a certain radius to that point are selected in order to decrease the number of leading points, and hence, to increase the speed of registration. This is realized by setting the importance function around the selected point to zero, after its selection.

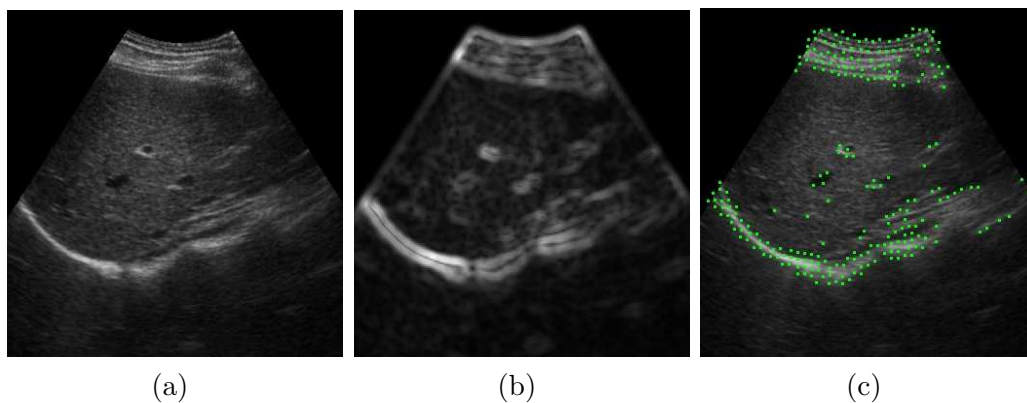


Fig. 2. (a) A 2D Ultrasound image of the liver, (b) Importance function, (c) Selected leading points

Figure 2(b) is the importance function of Figure 2(a) normalized between zero and one. The bright dots shown in Figure 2(c) are the selected leading points. As Figure 2(c) shows, the points are not evenly distributed; instead, they are mainly present in areas with distinguishable geometrical features such as the wall of the liver and the vessels. Considering the elements of the attribute

vector, it is expectable that the leading points are mostly located on the strong boundaries and the vessels. Other parts of images that are dominated by speckle patterns or are featureless may not be reliably registered. The images presented in Figure 2 are two dimensional, and are generated by the 2D version of our program to produce visually presentable images.

### 2.3 Matching

Let  $e_i(v)$  be the  $i$ 'th element of attribute vector assigned to voxel  $v$ . Then, the similarity of voxels  $v_1$  from the fixed image and  $v_2$  from the moving image is measured with:

$$Sim(v_1, v_2) = \prod_{i=1}^n (1 - \|e_i(v_1) - e_i(v_2)\|)^{w_i}, \quad (2)$$

where  $Sim(v_1, v_2)$  shows the similarity of attribute vectors at voxels  $v_1$  and  $v_2$ . The function is one for maximum similarity and zero for no similarity.  $w_i$  represents the same weight function as of Equation (1). If  $w_i$ 's are all set to one, all the elements of the attribute vector will make the same contribution towards determining the similarity.

To find the corresponding voxels in the fixed and moving images, the minimum of an energy function is found in a search area around the coordinates of the voxel in the fixed image. The energy function uses the described similarity function (Equation (2)) for several points around the two points; one from the fixed image and the other one from the moving image. The size of the search area is application dependent, and is directly proportional to the amount of deformation to be registered between the two data sets. For all of our experiments on actual images, we set the search radius to 20 voxels or 14.6 mm. The advantage of using a limited search area is that it reduces the computational complexity of the algorithm. Our energy function is similar to but not exactly the same as those defined in (Xiao et al. (2002); Shen and Davatzikos (2002)): Let  $p_i$  be the  $i$ 'th voxel in the neighborhood of the center point  $p$ , and  $q_j$  be the  $j$ 'th voxel in the neighborhood of the center point  $q$ . The energy function, when examining the correspondence of  $p$  and  $q$ , will be:

$$Eng(p, q) = \frac{\sum_i c(i)(1 - Sim(p_i, q_i))}{\sum_i c(i)} + \alpha d(p, q), \quad (3)$$

where  $c(i)$  is a convex weighting function which is maximum in the center of search area,  $d(p, q)$  is the distance of  $p$  from  $q$ , and  $\alpha$  is a small coefficient (set to 0.01 in our implementation). When the two sets of pixels  $p_i$  and  $q_i$  are similar, the energy function is minimized. The second term causes the

energy function to be minimum at closer points to the center, when there is no absolute minimum. The reason for adding this term is that when there are two candidates for the corresponding voxel, the probability that the closer voxel is the right choice is greater.

Due to shadowing effects and the nature of ultrasound images, it is possible that a feature disappears from one image to the other one. To counter this phenomenon, when a match is found, the energy function at the matching point should be below a threshold. Otherwise, that point is removed from the list of leading points. The value of the energy function in our experiments is normally around 0.2 for correct matches, and 0.8 or higher for false matches, respectively. Therefore, a threshold value close to 0.8 has been selected in our implementation.

#### 2.4 *Warping*

The final step of the registration process is the calculation of the movement of all the voxels of the moving image with respect to the fixed image, based on the calculated displacement of the leading feature points. The displacement of each voxel is mainly determined by the leading voxels that are close to that point. A Gaussian function displaces each leading voxel to adjoining points so that the displacement is faded through the neighbors. The variance of the function is set according to the image scale factors (in our set of experiments, the variance is set to 40 voxels). The selected leading voxels may be anywhere or distributed non-uniformly in the image, and there are no control points. Hence, spline-based techniques, which mainly require an evenly distributed set of grid points, have not been employed in the current implementation.

The contribution of each leading voxel to the displacement of one point is inversely proportional to the distance between the leading voxel and that point. The following equation is used in the warping process for voxel  $v$ :

$$Disp(v) = round\left(\frac{\sum_{i=1}^{n_{lead}} f_v(d_i)G(d_i)Disp(l_i)}{\sum_{i=1}^{n_{lead}} f_v(d_i)}\right), \quad (4)$$

where  $l_i$ 's are the leading voxels,  $n_{lead}$  is their number,  $d_i$  is the distance of  $v$  to  $l_i$ ,  $G$  is the Gaussian function that fades the effect of far leading voxels,  $f_v(d_i)$  is the inverse proportional function defined as  $1/(d_i^2 + \epsilon)$ , and  $\epsilon$  is a small positive number. The round function guarantees the displacement of each point to be an integer number. The inverse proportional function makes the weight to be very large for leading points, and the round function causes the leading points to be warped exactly to their corresponding voxels.

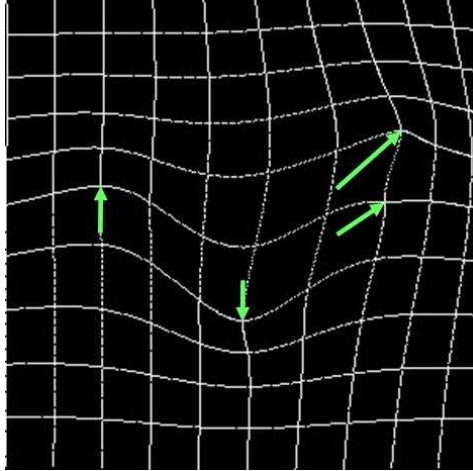


Fig. 3. The arrows show four arbitrary displacements, and the grid shows how the rest of the points are displaced with respect to these displacements.

To speed up the warping process, the Gaussian function is calculated and stored in a lookup table. The size of the table depends on the maximum expected displacement of the voxels  $D_{max}$  and the selected variance,  $\sigma$ , for the Gaussian function. To ensure smoothness, the size should be greater than the radius in which the maximum displacement of the leading points affects the displacement of other voxels. In other words, the table should be sufficiently large such that, in the case of maximum deformation, the farthest voxel affected would incur displacement of one voxel or no displacement, that is:

$$D_{max}e^{-\frac{r^2}{2\sigma^2}} \leq 1, \quad (5)$$

where  $r$  is the suitable radius for the lookup table. From Equation (5), the minimum radius for the Gaussian function to be calculated will be:

$$r_{min} = \sigma\sqrt{2\ln(D_{max})}. \quad (6)$$

Equation (6) can be applied to each of  $X$ ,  $Y$ , and  $Z$  directions separately. Hence, the dimensions of the lookup table may not be equal.

Figure 3 shows how the points in the image are displaced as a result of four arbitrary displacements. Since the leading points are not evenly distributed throughout the images, and are not necessarily placed on the vertices of a grid, conventional methods cannot be used for warping. As Figure 2(c) shows, the leading points can be very close to each other or far apart. The selected method is not only a good approximation of the deformation, but also a fast method for extrapolating the movement of the leading points.

### 3 Results

The algorithm has been implemented in MATLAB<sup>TM</sup>. The matching and warping parts are written in C, and compiled with the C compiler of MATLAB<sup>TM</sup> to reduce the computation time. Two sets of tests were carried out in order to evaluate the accuracy, robustness, and speed of the technique. First, actual 3D ultrasound images were captured, and registered to each other. Registration of naturally deformed images is the best method for testing the performance of the registration algorithm since some issues, such as motion ambiguities and speckle decorrelation (Pratikakis et al. (2001)), are not present in simulation experiments. However, simulation experiments help to evaluate the accuracy of registration since exact deformations are unknown for actual images. Hence, in the second set of tests, the ultrasound volumes were elastically deformed by a known displacement matrix. The original and deformed volumes were then registered to each other.

#### 3.1 *Experimental Results*

Ultrasound images were captured by a GE Voluson 730 3D/4D ultrasound machine. The RAB4-8P transducer was used to collect 3D images from six volunteers' livers, and the images were saved in Cartesian format. These images were captured at multiple locations under different forces applied to the abdomen by a variety of operator hand pressures on the transducer. The deformation in ultrasound volume data sets was caused by transducer pressure, respiration, heartbeat, and changes in the physical position of the volunteers. For each volunteer, five sets of images were captured. Each set of images consisted of two volumes –at two different moments of the breathing cycle– which were taken from one area of the volunteer's liver. For each set, one of the volumes was selected as the fixed image, and the other one (moving image) was registered to it. Registration parameters were kept identical for all experiments. The average initial displacement between the images in each set was estimated to be 6 millimeters with a maximum displacement of 14.6 millimeters.

Figures 4(a,b,c) demonstrate one slice of the fixed, moving and registered data sets. The difference images shown in Figures 4(d,e) depict the accuracy of the alignment of features after registration. It should be noted that the registration is performed in 3D, hence some out-of-plane features, which may not exist in the demonstrated moving and fixed images, have been warped to the shown registered slice. Three slices in three orthogonal planes from two other experiments are demonstrated in Figures 5 and 6. The circles and arrows are at the same coordinates for all images in each row to show how the main

anatomical features, like liver boundaries and vessels, are matched.

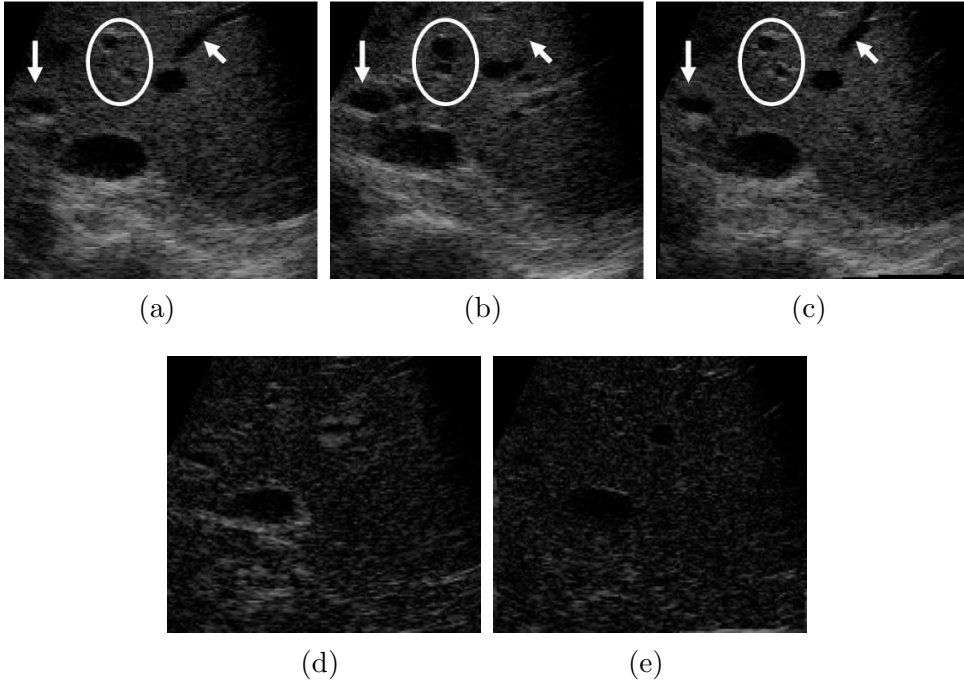


Fig. 4. (a) is a middle slice of the fixed volume, (b) is the same slice in the moving volume, and (c) is the same slice in the registered volume. (d) shows the absolute of difference between the fixed and the moving volumes, and (e) is the absolute of difference between the fixed and the registered volumes.

We were unable to find any quantitative method for evaluating the elastic registration of ultrasound images taken from real subjects in the literature. The reason is that the deformation of soft tissue inside the human body is unknown for the given images. On the other hand, segmentation of ultrasound images of soft tissue such as liver is very difficult, and the accuracy of the segmentation could be questioned. Therefore, segmentation could not be easily used as a tool for evaluating the results. However, it is crucial to check the performance of registration for naturally deformed images. To evaluate the performance, eight voxels on distinct features of the fixed and the registered volumes were manually selected. This selection was performed independently for each set of volume used. The selected landmarks in two separate volumes from two subjects are shown in Figure 7. The only points selected were those where the operator could confidently locate their corresponding point on the deformed image. It was not possible to choose certain anatomical features that are common in most human livers because the images were taken from different locations of the liver under varying conditions. The distance between these manually selected points in the fixed and the moving data sets, after the automatic registration, was considered as the error at that point. Using this method, the average error of registered images was about 1.4 millimeters, which is about 77 percent correction, considering the uncertainties in the images and their poor quality.

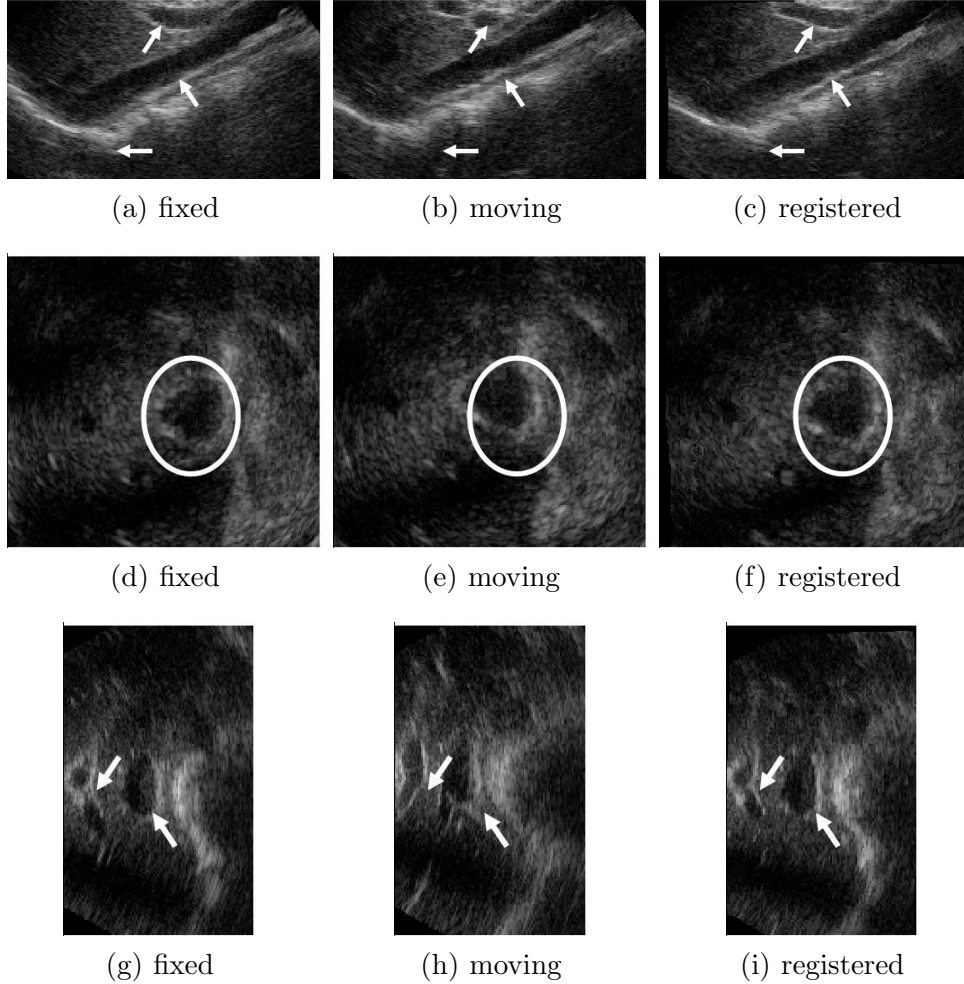


Fig. 5. (a),(b), and (c) are the slices of fixed, moving and registered volumes, parallel to ZY plane; (d) to (f) are the slices parallel to ZX plane, and (g) to (i) are the slices parallel to XY plane.

### 3.2 Simulation Results

In the second set of experiments, the matrices of displacement vectors, generated by the registration of naturally deformed images in the previous section, were used to simulate elastic deformations. The original volumes were then registered to the deformed volumes, and the results were compared to the original displacement matrices. To adjust the average deformation, the displacement matrices were multiplied by a constant scale factor. The average of mean registration error for 30 volumes deformed with 30 different displacement matrices was 1.30 mm for an average initial displacement of 7.4 mm between the volume sets. Figure 8 represents three planes of one displacement matrix orthogonal to  $z$  axis. The planes are 20 voxels apart from each other. The white grid shows the deformation in  $x$  and  $y$  directions, while the intensity of the images represents the deformation in  $z$  direction.

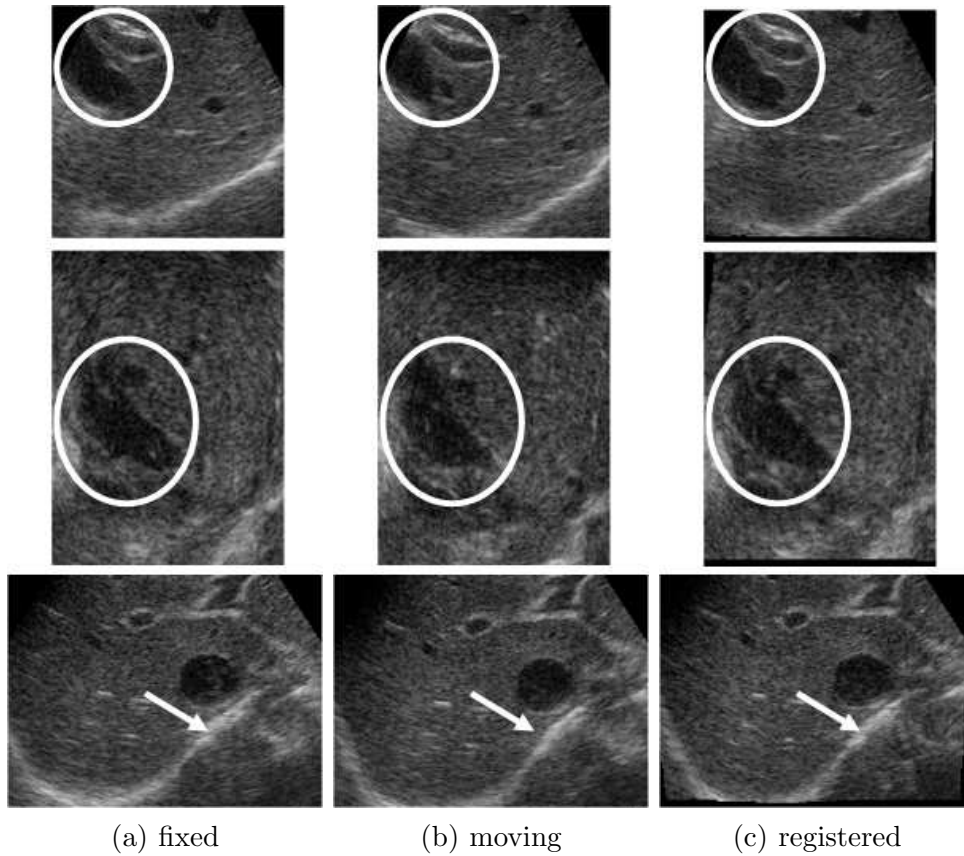


Fig. 6. Similar to Figure 5, three perpendicular slices of the fixed, moving, and registered volumes are depicted. The figure shows how different anatomies –like the boundary of liver and vessels– are registered. The circles and arrows are at the same location for all the images in each row.

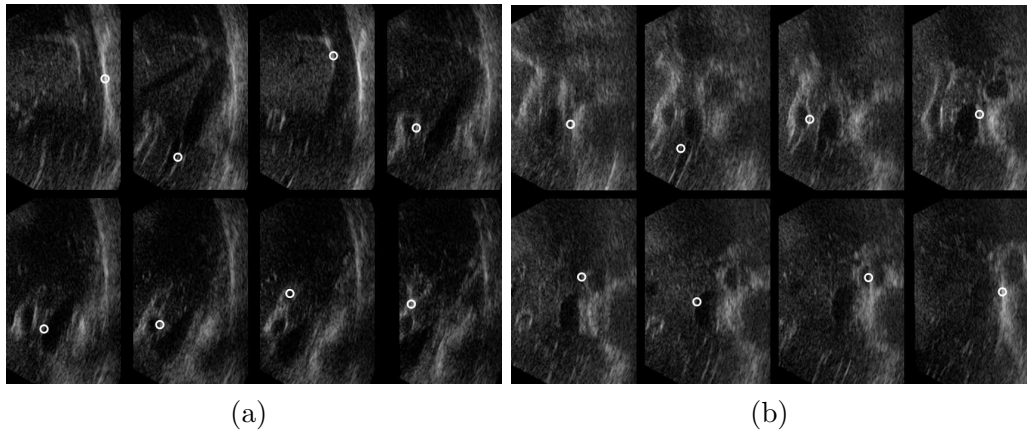


Fig. 7. The eight slices on which the landmarks are manually selected to verify the registration accuracy, are shown for two volumes from two subjects. The centers of the circles show the selected points.

Figure 9(a) is the histogram of a displacement matrix with an average initial displacement of 10.6 voxels, applied to an ultrasound volume of 149x145x199

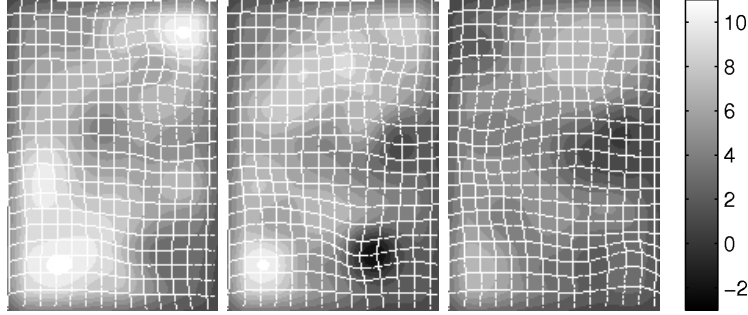


Fig. 8. Three planes of one displacement matrix orthogonal to  $z$  axis 20 voxels apart from each other. The white grid shows the deformation in  $x$  and  $y$  directions, while the intensity of the images represents the deformation in  $z$  direction. The range of displacement in  $z$  direction is from -3 to 11 voxels.

voxels with scale factor of 0.7 mm. After registering the images, the calculated displacement matrix is compared to the original, and registration error vectors are computed. Figure 9(b) is the histogram of the magnitude of registration error vectors. For this experiment, the average registration error is 1.9 voxels or 1.3 mm.

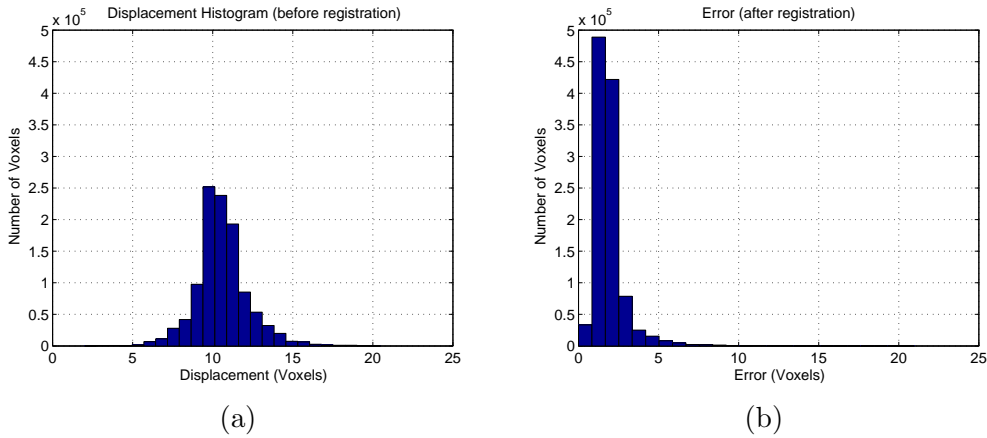


Fig. 9. (a) is the histogram of displacements before registration, and (b) is the histogram of the magnitudes of error vectors after registration.

## 4 Discussion

For a successful registration, the correct values for the parameters of the algorithm should be selected. This section investigates the effect of these parameters on registration results and the sensitivity of the registration to the parameters. Moreover, additional experiments are provided to show the discrimination ability of the proposed attribute vector and to compare the performance of the proposed vector elements with the GMIs for ultrasound images.

Table 1

The simulation experiment was carried out for a 185x113x199 ultrasound volume of a liver using a Pentium 4 2.8GHz CPU. average initial displacement of the deformation matrix was 13.02 voxels or 9.24 mm, and the maximum displacement was 27.71 voxels. The table highlights the algorithm’s sensitivity to the threshold used for the selection of leading points.

Threshold	Number of LPs <sup>1</sup>	Time to Register LPs <sup>1</sup> (Sec)	Time to Warp (Sec)	Mean Error (voxels)	Correction Percentage
0.6	5	9.76	4.80	6.47	50
0.4	21	40.61	9.95	3.97	70
0.3	33	63.72	14.24	3.48	73
0.2	62	120.02	20.77	2.57	80
0.18	70	135.20	22.86	2.38	82
0.16	79	152.42	25.20	2.33	82
0.14	85	163.99	26.84	2.45	81
0.12	95	183.48	29.40	2.44	81
0.1	105	202.81	32.46	2.49	81

#### 4.1 The Effect of Parameters

The number of leading points is not constant for the images and is determined by a threshold. Sufficient number of leading points should be selected to ensure successful registration. Table 1 reports the simulation results for different thresholds used for the selection of leading points. The table shows that, for high values of the threshold, when an insufficient number of leading points is selected, the performance decreases. For lower threshold values, additional leading points are selected, but the registration time increases. However, when enough leading points are selected, increasing their number does not affect the results much. This also means that the registration is not very sensitive to this threshold. The threshold value for all previous experiments was set at 0.14. It should be noted that this threshold value cannot be very low since a selection of too many leading points would impair the performance because points that cannot be registered robustly will be selected as leading points.

In our proposed algorithm, the leading points cannot be closer to each other than a selected radius. Changing this radius affects both the error and the number of selected leading points for one simulation, as shown in Table 2. Increasing this radius decreases the number of selected leading points and consequently increases the registration speed, but the error also increases. To

<sup>1</sup> Leading Points

reduce the chance of intersecting leading points, this number should be greater than the expected mean error. In the current implementation, we do not check for intersections among leading points.

Table 2

The effect of changing the radius around leading points on the registration error and the number of selected leading points.

LP Radius (voxel)	Mean Error (voxels)	Number of LPs
2	1.38	55
4	1.36	31
6	1.47	17
8	1.42	16
10	1.55	12
12	1.63	7
14	1.85	5
16	2.15	5

The most important parameter to set is the radius of the search area, which determines the size of the region around the leading points, where the algorithm expects to find the corresponding point. Figure 10 demonstrates the change of mean error over the search radius for five simulations. As depicted in Figure 10, if the radius is improperly selected, some of the leading points are improperly registered and the error dramatically increases. Nonetheless, a very large radius slightly increases the error because there would be a higher chance of failure in the registration of leading points.

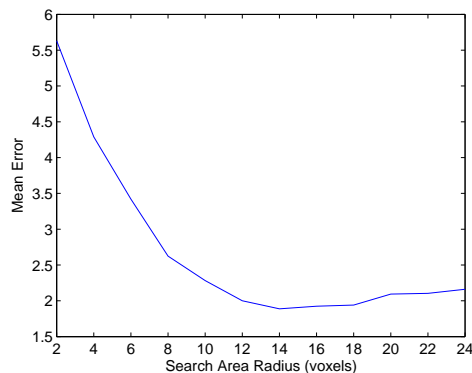


Fig. 10. The effect of increasing the search radius on the average registration error.

Finally, the weight of the elements of the attribute vector can play an important role in the selection of leading points. As previously mentioned, the weight of the magnitude of the gradient is selected to be twice the other ones, as it

is the most effective feature of the attribute vector. We studied the effect of including LoG, as of the attribute vector elements, on the registration results. To this end, we performed two independent set of simulations on 30 volume sets; one including LoG in, the other excluding LoG from the attribute vector calculation. The mean registration error of 1.89 voxels, when including LoG, increased to 2.01 voxels (around 6% increase) when LoG was excluded, which is not significant. However, we prefer to present the algorithm in its general format and to include this element in the set of our features as it considers cases where faded edges or shadows exist in the images. Since the calculation of LoG does not in fact require much computation time, this inclusion should not significantly affect the reported execution times.

#### 4.2 Error Pattern and the Effect of Shadow

Ultrasound waves cannot pass through certain tissues of the body –especially bones– that causes shadows in the images. No leading point is selected from a featureless area of the image such as a shadowed area. Therefore, the deformation for that part of the image is estimated from the adjacent leading points. However, the estimation of the deformation becomes less reliable when the featureless area is far from the leading points. Figure 11(a) shows one slice of a volume from one of our simulation experiments, in which a section of the image is dark. The program is forced to select all the leading points from this slice to prevent the interference from other leading points from other slices in the registration result, and to enable us to study the error pattern presented in a 2D image (Figure 11(b)). The white dots in Figure 11(b) represent the location of the selected leading points. No leading point is selected in the shadowed area which has resulted in less accurate deformation estimation for that featureless area.

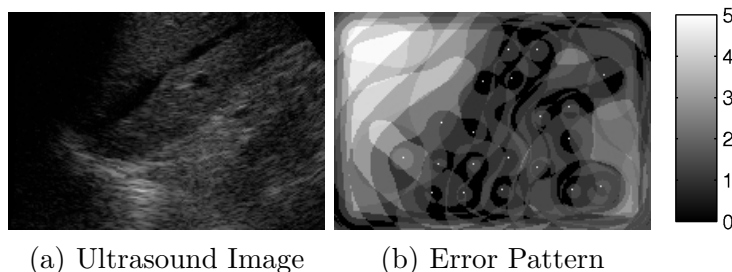


Fig. 11. The program is forced to select all the leading points from the slice shown in (a). The registration error pattern is shown in (b). The white dots represent the location of leading points.

There is a slim possibility that the shadow only appears in one of the two images. To check the robustness of the registration for this situation, a set of new images were collected. In these new data sets, a fixed image was first

collected. Afterwards, a barrier was placed between the transducer and the subject’s skin in order to create a shadow in the moving image. Figure 12 shows the registration results for one such case. The registration seems to be visually acceptable when the major anatomical features are not covered, but there is no practical way to quantitatively determine the registration accuracy for the shadowed area since the experiments are for naturally deformed data.

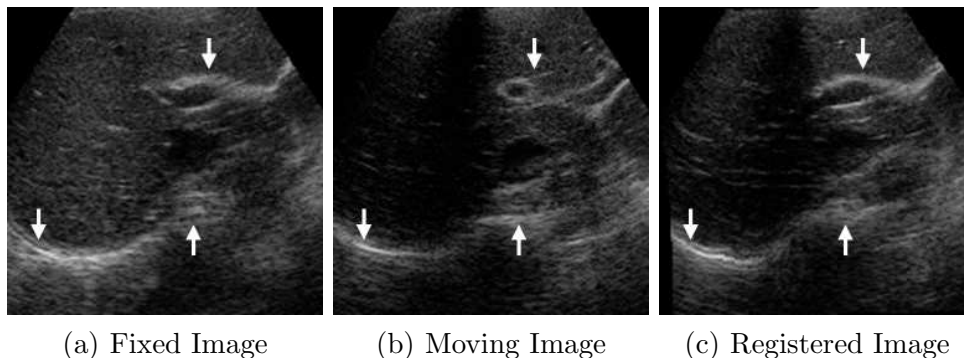


Fig. 12. The moving image is shadowed by placing a barrier between the transducer and the subject’s skin. The registration result is not largely affected by the shadow. The error range is from 0 voxels for dark areas to 5 voxels. The white arrows are at the same position in all images.

### 4.3 Discrimination Ability of Proposed Attribute Vector

Figure 13 illustrates the similarity of the first selected leading point on the fixed image with all the points in one slice of the moving image. The selected slice is where the similarity is maximum for the whole image. The white arrow on Figure 13(a) points to the first selected leading point. Figure 13(c) shows the similarity of this point with all the points of the deformed volume on the slice where the similarity is maximum. The figure shows that, for this case, the matched point (in the moving image) to the selected leading point (in the fixed image) is clearly distinguishable from the remainder of the points in the moving image.

However, this result is not usually replicated for all the selected leading points. As more points are selected, the discrimination ability of the points decreases, and therefore, the accuracy of the registration of the points drops. The average accuracy of the first 60 leading points for five simulations is reflected in Table 3. The table suggests that, on average, the first selected leading points are registered more accurately, which implies that the selected points are proper for registration.

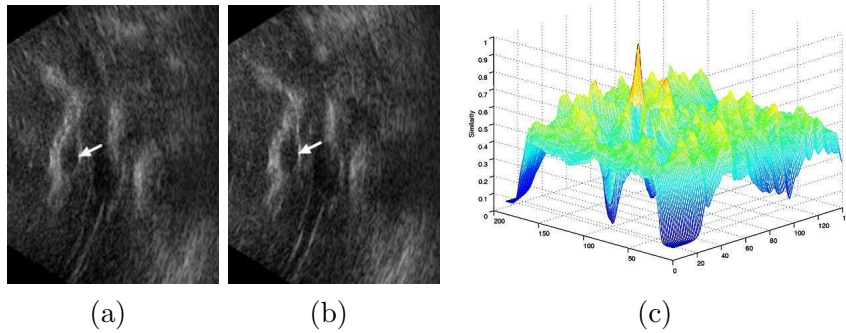


Fig. 13. (a) and (b) are one slice of the fixed and moving images, respectively. The white arrow on (a) is the first selected leading point, and the one on (b) is the corresponding voxel with highest similarity. (c) shows the similarity of the leading point on (a) with all the points of image (b).

Table 3

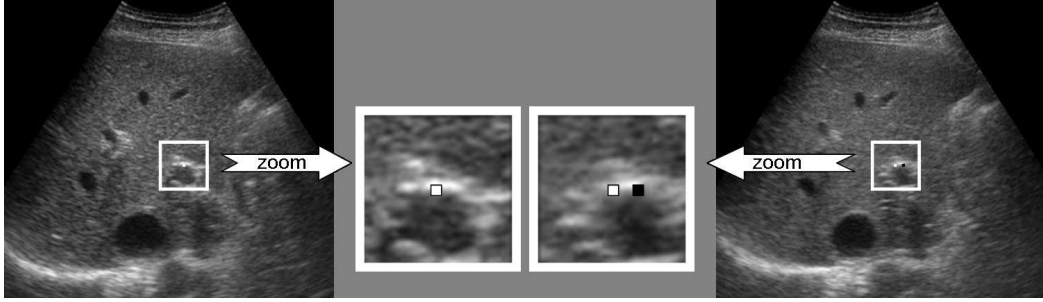
The average registration accuracy of first 60 leading points for five simulations

	LPs 1-20	LPs 21-40	LPs 41-60
Average Accuracy (voxels)	1.65	1.75	2.02

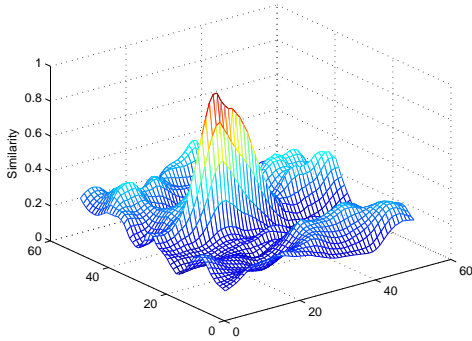
#### 4.4 Comparison with GMIs

Figure 14 compares the discrimination ability of the proposed attribute vector with the attribute vector composed of GMIs. The middle left image in Figure 14(a) measures the similarity of the six-pixel radius area beneath the bright filled-in square with all the points of its middle right counterpart. The similarity measures are summed up and shown for each center point. The black filled-in square on the middle right image corresponds to the bright filled-in square. Figure 14(b) depicts the calculated similarities using the proposed attribute vector, while Figure 14(c) portrays the best results obtained using the GMIs. To derive maximum results for GMIs, the radius of calculation of geometric moments was set to 15 pixels and the GMIs were calculated over two scales. The peaks of the graphs in Figures 14(b) and 14(c) are the points with the highest similarity measure. In Figure 14(b), the corresponding point is clearly distinguished from the rest of points, in comparison with Figure 14(c), where the similarity measure of local maxima is close to the absolute maximum. Although our proposed attribute vector requires around fifteen times less computing time, our experiments under different conditions show that it outperforms GMI in discrimination of ultrasound image features.

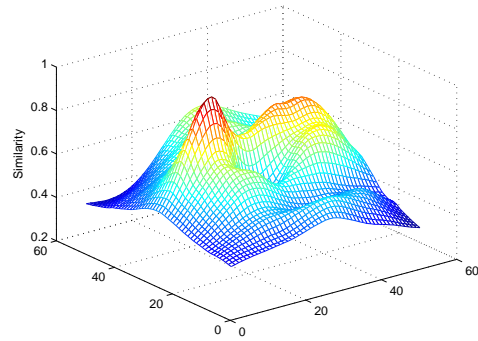
To make a quantitative comparison, we replaced our attribute vector with GMIs up to third order. The intensity of the voxel was also added to the vector to improve the results. The mean error of 30 simulations was increased from 1.86 voxels to 3.83 voxels using this set of elements, which suggests the superiority of the proposed set of elements for ultrasound images.



(a)



(b)



(c)

Fig. 14. (a) The two middle images are the zoomed images of the two areas surrounded by white squares on the side images. The bright filled-in squares on the zoomed images are at the same location, and the black square on the middle right image corresponds to the bright square on the middle left image. Graph (b) shows the similarity of the white square with all the points in the rectangle using the proposed attribute vector, while (c) is the similarity measure with the GMIs

## 5 Conclusion and Future Work

We have developed a method for 3D elastic registration of ultrasound images, which is intended eventually for radiotherapy and surgical applications. The algorithm does not require presegmentation or numerical optimization resulting in relatively shorter running time. A number of experiments were carried out using naturally and artificially deformed ultrasound images of liver showing clinically acceptable accuracy. Detailed analyses were also provided on the selection of parameters for the algorithm and on the discrimination ability of the proposed attribute vector. Future work will include improving performance by developing a method for failure detection of registration of leading points, as well as improving the normalization strategies. In addition, the code could be optimized to reduce the running time of the algorithm to within an acceptable range for intra-operative applications. Real-time implementation also seems to be achievable by exploiting hardware acceleration. Finally, the algorithm should be tested for the registration of ultrasound images of other

anatomical parts in addition to the liver.

## References

- Arbel, T., Morandi, X., Comeau, R. M., Collins, D. L., October 2001. Automatic nonlinear MRI-ultrasound registration for the correction of intra-operative brain deformations. In: *Medical Image Computing and Computer Assisted Intervention*. pp. 565–572.
- Aylward, S. R., Jomier, J., Guyon, J. P., Weeks, S., July 2002. Intra-operative 3D ultrasound augmentation. In: *IEEE International Symposium on Biomedical Imaging*. pp. 421–424.
- Blackall, J. M., Penney, G. P., King, A. P., Hawkes, D. J., November 2005. Alignment of sparse freehand 3-D ultrasound with preoperative images of the liver using models of respiratory motion and deformation. *IEEE Trans. Image Process.* 24 (11), 1405–1416.
- Foroughi, P., Abolmaesumi, P., October 2005. Elastic registration of 3d ultrasound images. In: *Medical Image Computing and Computer Assisted Intervention*. pp. 83–90.
- Groves, A., Rohling, R., 2004. Two-dimensional spatial compounding with warping. *Ultrasound Med. Biol.* 30 (7), 929–942.
- Hajnal, J. V., Hill, D. L. G., Hawkes, D. J., 2001. *Medical Image Registration. The Biomedical Engineering Series.* CRC Press.
- Hill, D. L. G., Batchelor, P. G., Holden, M., Hawkes, D. J., 2001. Medical image registration. *Phys. Med. Biol.* 46 (3), R1–R45.
- King, A. P., Blackall, J. M., Penney, G. P., Edwards, P. J., Hill, D. L. G., Hawkes, D. J., October 2000. Bayesian estimation of intra-operative deformation for image-guided surgery using 3-D ultrasound. In: *Medical Image Computing and Computer Assisted Intervention*. pp. 588–597.
- King, A. P., Blackall, J. M., Penney, G. P., Hawkes, D. J., Desember 2001. Tracking liver motion using 3-D ultrasound and a surface based statistical shape model. In: *Mathematical Methods in Biomedical Image Analysis*. pp. 145–152.
- Krucker, J. F., LeCarpentier, G. L., Fowlkes, J. B., Carson, P. L., 2002. Rapid elastic image registration for 3-D ultrasound. *IEEE Trans. Med. Imaging* 21 (11), 1384–1394.
- Ledesma-Carbayo, M. J., Kybic, J., Desco, M., Santos, A., Unser, M., October 2001. Cardiac motion analysis from ultrasound sequences using non-rigid registration. In: *Medical Image Computing and Computer Assisted Intervention*. pp. 889–896.
- Letteboer, M. M. J., Willems, P. W. A., Viergever, M. A., Niessen, W. J., February 2005. Brain shift estimation in image-guided neurosurgery using 3-D ultrasound. *IEEE Trans. Biomed. Eng.* 52 (2), 268–276.

- Maintz, J. B. A., Viergever, M. A., 1998. A survey of medical image registration. *Med. Image Anal.* 2 (1), 1–36.
- Makela, T., Clarysse, P., Sipila, O., Pauna, N., Pham, Q. C., Katila, T., Magnin, I. E., September 2002. A review of cardiac image registration methods. *IEEE Trans. Med. Imaging* 21 (9), 1011–1021.
- Meyer, C. R., Boes, J. L., Kim, B., Bland, P. H., Zasadny, K. R., Kison, P. V., Koral, K., Frey, K. A., Wahl, R. L., 1997. Demonstration of accuracy and clinical versatility of mutual information for automatic multimodality image fusion using affine and thin-plate spline warped geometric deformations. *Med. Image Anal.* 1 (3), 195–206.
- Pagoulatos, N., Edwards, W. S., Haynor, D. R., Kim, Y., December 1999. Interactive 3D registration of ultrasound and magnetic resonance images based on a magnetic position sensor. *IEEE Trans. Inf. Technol. Biomed.* 3 (4), 278–288.
- Pluim, J. P. W., Fitzpatrick, J. M., November 2003. Image registration. *IEEE Trans. Image Process.* 22 (11), 1341–1343.
- Poon, T. C., Rohling, R. N., 2006. Three-dimensional extended field-of-view ultrasound. *Ultrasound Med. Biol.* 32 (3), 357–369.
- Pratikakis, I., Barillot, C., Hellier, P., 2001. Robust multi-scale non-rigid registration of 3D ultrasound images. In: *Scale-Space*. pp. 389–397.
- Rohling, R. N., Gee, A. H., Berman, L., 1998. Automatic registration of 3-D ultrasound images. *Ultrasound Med. Biol.* 24 (6), 841–854.
- Shekhar, R., Zagrodsky, V., 2002. Mutual information-based rigid and nonrigid registration of ultrasound volumes. *IEEE Trans. Med. Imaging* 21 (1), 9–22.
- Shekhar, R., Zagrodsky, V., Garcia, M. J., Thomas, J. D., 2004. Registration of real-time 3-D ultrasound images of the heart for novel 3-D stress echocardiography. *IEEE Trans. Med. Imaging* 23 (9), 1141–1149.
- Shen, D., September 2004. Image registration by hierarchical matching of local spatial intensity histograms. In: *Medical Image Computing and Computer Assisted Intervention*. pp. 582–590.
- Shen, D., Davatzikos, C., 2002. Hammer: hierarchical attribute matching mechanism for elastic registration. *IEEE Trans. Med. Imaging* 21 (11), 1421–1439.
- Xiao, G., Brady, M., Noble, J. A., Burcher, M., English, R., 2002. Nonrigid registration of 3-D free-hand ultrasound images of the breast. *IEEE Trans. Med. Imaging* 21 (4), 405–412.